Linear stability analysis of the onset dynamics of scramjet unstart

By I. Jang, P. Moin AND J. W. Nichols†

1. Motivation and objectives

Recently, interest has increased in using scramjet engines as a means of long-range high-speed flights and economical access to outer space. One of the most perilous causes of scramjet malfunctions is the unstart event that is initiated by excessive heat release from combustion. When unstart occurs, a strong moving-shock structure is first formed in the engine, and the shock structure propagates upstream and finally spills out of the engine inlet. The unstart event is detrimental to the engine because (1) the moving-shock structure imposes high pressure and thermal loads on the inner walls of the engine during the unstart process, and the walls can be ruptured due to the loads; and (2) the airflow into the engine is greatly diminished when the shock structure is disgorged by the engine, leading to loss-of-thrust and engine stall. Because the probability of unstart grows with increasing heat release from combustion, the danger of unstart is an important limiting factor in the performance of scramjets.

Therefore, the onset mechanisms of the unstart event need to be understood to prevent or delay the unstart process. However, the detailed dynamics has not been fully understood yet, even though many studies have examined unstart onset mechanisms. For instance, Korkegi (1975) suggested empirical correlation functions for estimating the critical pressure rise above which unstart occurs, based on the assumption that shock-induced flow separation of turbulent boundary layers on the engine walls causes the unstart process. In ground tests of the HyShot II scramjet model (Frost *et al.* 2009), the critical pressure rise in the model agreed with the Korkegi limit, and therefore the authors presumed that unstart was initiated by flow separation of the boundary layers. In a later ground experiment of HyShot II, however, Laurence *et al.* (2013) could not find large-scale boundary-layer separations, and they concluded that flow separation was not the main cause of unstart. Instead, they proposed thermal choking as the responsible unstart mechanism. However, further conclusions regarding the onset mechanism could not be drawn because of the limited diagnostics in the experiments.

The primary objective in this study is to find the onset dynamics of the unstart event based on linearized system. Section 2 describes the linearized system dynamics that will be discussed throughout this study. In section 3, the detailed methodology and the scramjet configuration are presented. The linearized dynamics at the unstart onset point is then discussed in section 4. Finally, section 5 summarized the findings and make suggestions for future work.

† Aerospace Engineering Department, University of Minnesota, Minneapolis MN

2. Linearized dynamics of a scramjet system

In this study, we consider the dynamic system of the following form:

$$\frac{d\boldsymbol{w}}{dt} = \boldsymbol{F}(\boldsymbol{w};\phi), \quad \boldsymbol{w} = [\rho, \rho\boldsymbol{u}, \rho E, \text{scalars}]^T, \tag{2.1}$$

where ϕ is an adjustable input parameter to the system, $\boldsymbol{w}$ is a solution vector describing the system state, and $\boldsymbol{F}$ is a non-linear map describing the temporal evolution of the system state. In this study, we consider supersonic flows in a model scramjet with a heat source. Therefore, $\boldsymbol{F}$ is the compressible Navier-Stokes equations with a turbulent model, and ϕ is the heat release rate of the source. $\boldsymbol{w}$ is the flow variable vector whose elements are density (ρ), the momentum vector ($\rho\boldsymbol{u} = [\rho u_1, \rho u_2, \rho u_3]^T$), total energy ($\rho E$), and conservative scalars in the turbulent model. Because the Wilcox $k-\omega$ turbulent model (Wilcox 2006) is used in this study, the conservative scalars are k and ω. Because computational grids are used to represent the flow field, the dimension n of the vector $\boldsymbol{w}$ in the computation is $N_{\text{grids}} \times N_{\text{vars}}$, where N_{grids} is the number of the grid points and N_{vars} is the number of flow variables at each grid point. In this study, N_{vars} is 7: density (ρ), the three components in momentum ($\rho\boldsymbol{u}$), total energy (ρE), and the two scalars in the $k-\omega$ RANS model (ρk and $\rho\omega$). Similarly, the dimension of the vector function $\boldsymbol{F}$ is equal to n. Therefore, the phase space of this dynamical system comprises total $(n+1)$-dimensional space. The trajectory of the solution evolves in time and in the phase space from an initial solution in $\boldsymbol{w}$ and ϕ. In general, the system input parameter ϕ is assumed to be given and fixed, and in this case, an n-dimensional phase space only for $\boldsymbol{w}$ is considered.

In this study, we are particularly interested in equilibrium solutions and in the dynamics near the equilibria. An equilibrium solution $\boldsymbol{w_0}(\phi)$ at a given parameter ϕ satisfies

$$\boldsymbol{F}(\boldsymbol{w_0};\phi) = 0. \tag{2.2}$$

In general, the equilibrium solution set forms a continuous curve in the phase space. The dynamics near an equilibrium solution $(\boldsymbol{w_0};\phi_0)$ can be expressed in the following linearized system:

$$\frac{d\boldsymbol{w'}}{dt} = \mathcal{A}_{(\boldsymbol{w_0};\phi_0)}\boldsymbol{w'}. \tag{2.3}$$

In this linearized system, $\boldsymbol{w'} \in \mathbb{R}^n$ is a perturbation vector from an equilibrium $\boldsymbol{w_0}(\phi_0)$, where ϕ_0 is assumed to be a constant value. $\mathcal{A}_{(\boldsymbol{w_0};\phi_0)} \in \mathbb{R}^{n\times n}$ is the Jacobian matrix of $\boldsymbol{F}$, evaluated at the equilibrium solution, $(\boldsymbol{w_0};\phi_0)$:

$$\mathcal{A}_{(\boldsymbol{w_0};\phi_0)} = \nabla_{\boldsymbol{w}}\boldsymbol{F}(\boldsymbol{w_0};\phi_0) = [a_{i,j}], \quad a_{i,j} = \left(\left.\frac{\partial \boldsymbol{F}_i}{\partial \boldsymbol{w}_j}\right|_{(\boldsymbol{w_0};\phi_0)}\right)_{i,j}. \tag{2.4}$$

The eigen-decomposition of $\mathcal{A}_{(\boldsymbol{w_0};\phi_0)}$ plays an important role in explaining the system dynamics. Let $\lambda_1, \lambda_2, \cdots, \lambda_n$ be eigenvalues of $\mathcal{A}_{(\boldsymbol{w_0};\phi_0)}$ and $\boldsymbol{y}_1, \boldsymbol{y}_2, \cdots, \boldsymbol{y}_n$ be the associated direct global modes (or right eigenvectors). In other words, each pair of λ_i and $\boldsymbol{y}_i$ satisfies

$$\mathcal{A}_{(\boldsymbol{w_0};\phi_0)}\boldsymbol{y}_i = \lambda_i\boldsymbol{y}_i, \qquad i = 1, \cdots, n. \tag{2.5}$$

Here, λ_i's are scalars, and $\boldsymbol{y}_i$'s are n-dimensional vectors. For complex λ_i's, the corresponding $\boldsymbol{y}_i$'s are also complex. Without loss of generality, it can be assumed that $\text{Re}(\lambda_1) \geq \text{Re}(\lambda_2) \geq \cdots \geq \text{Re}(\lambda_n)$. The real part of an eigenvalue stands for the growth rate of the corresponding mode in time, whereas the imaginary part is related to the

oscillatory dynamics. Therefore, λ_1 is the least stable because its associated global mode grows the fastest in time (if $\mathrm{Re}(\lambda_1) > 0$) or decays the slowest in time (if $\mathrm{Re}(\lambda_1) < 0$). If all the eigenvalues of $\mathcal{A}_{(\boldsymbol{w_0};\phi_0)}$ have a negative real part, any point in a neighbor of $(\boldsymbol{w_0};\phi_0)$ is stable. On the other hand, if few eigenvalues have a zero real part, the system is marginally stable.

3. Methodology and configurations

3.1. *Calculation of the solution curve*

In this study, the pseudo-arclength continuation method (Keller 1977; Chan & Keller 1982) is applied to obtain the solution curve. In the pseudo-arclength continuation algorithm, an additional equation called the "tangential condition" is added to $\boldsymbol{F}(\boldsymbol{w};\phi)$ in Eq. (2.1). To obtain the $(k+1)$th solution point, two previous solutions, $\boldsymbol{z}^{k-1} = (\boldsymbol{w^{k-1}};\phi^{k-1})$ and $\boldsymbol{z}^k = (\boldsymbol{w^k};\phi^k)$ are first stored. Because the dimension of $\boldsymbol{w}$ and ϕ are n and 1, respectively, the dimension of $\boldsymbol{z}$ is equal to $n+1$. Using these two solution vectors, a tangential vector $\boldsymbol{t} = \boldsymbol{z}^k - \boldsymbol{z}^{k-1}$ and the pseudo-arclength $\Delta_s = ||\boldsymbol{z}^k - \boldsymbol{z}^{k-1}||_2$ are calculated. Here, $||\boldsymbol{v}||_2$ stands for the two-norm of a vector $\boldsymbol{v}$. Then, the next solution $\boldsymbol{z}^{k+1}$ is searched on a plane that satisfies both of the following conditions: (1) the extrapolated point $\boldsymbol{z}^k + \boldsymbol{t}$ should be on the plane, and (2) the tangential vector of the plane is equal to $\boldsymbol{t}/\Delta_s$. In order for $\boldsymbol{z}^{k+1}$ to be on such a plane, $\boldsymbol{z}^{k+1}$ must satisfy the tangential condition, $T(\boldsymbol{z}^{k+1}, \boldsymbol{t}, \Delta_s) = \boldsymbol{t}^T(\boldsymbol{z} - \boldsymbol{z}^k)/\Delta_s - \Delta_s = 0$.

During the search process for $\boldsymbol{z}^{k+1}$, the Newton iterative method is used (Allgower & Georg 1997). When the tangential condition is included, the non-linear system is expressed by the vector function

$$\boldsymbol{G}(\boldsymbol{z}) = \begin{bmatrix} \boldsymbol{F}(\boldsymbol{z}) \\ T(\boldsymbol{z}^{k+1}, \boldsymbol{t}, \Delta_s) \end{bmatrix} \in \mathbb{R}^{n+1},$$

and $\boldsymbol{z}^{k+1}$ is the root of $\boldsymbol{G}(\boldsymbol{z}) = 0$. At each Newton iteration step, the solution is updated by $\boldsymbol{z} := \boldsymbol{z} + \alpha\Delta\boldsymbol{z}$, where α is a step size, and $\Delta\boldsymbol{z}$ is a search direction. The range of α is $0 < \alpha < 1$, and it is determined based on the three-point parabolic method (Kelley 1995). $\Delta\boldsymbol{z}$ is given as $\Delta\boldsymbol{z} = -\mathcal{B}_{\boldsymbol{z}}^{-1}\boldsymbol{G}(\boldsymbol{z})$, where

$$\mathcal{B}_{\boldsymbol{z}} = \begin{bmatrix} \mathcal{A}_{\boldsymbol{z}} & (\nabla_\phi \boldsymbol{F})_{\boldsymbol{z}} \\ & \boldsymbol{t}^T \end{bmatrix} \in \mathbb{R}^{(n+1)\times(n+1)},$$

and $\mathcal{A}_{\boldsymbol{z}}$ is the Jacobian matrix of the vector function $\boldsymbol{F}$ evaluated at $\boldsymbol{z}$. The stopping criterion of the Newton iteration is $||\boldsymbol{G}(\boldsymbol{z})||_2 \leq \epsilon_{\mathrm{abs}}$ or $||\boldsymbol{G}(\boldsymbol{z})||_2/||\boldsymbol{G}(\boldsymbol{z}^k + \boldsymbol{t})||_2 \leq \epsilon_{\mathrm{rel}}$, where ϵ_{abs} and ϵ_{real} are the absolute threshold and the relative threshold, respectively. In this study, the threshold values are $\epsilon_{\mathrm{abs}} = 10^{-6}$ and $\epsilon_{\mathrm{rel}} = 3 \times 10^{-11}$. After satisfying the stopping criterion, three more Newton iterations are performed to ensure convergence.

In order to prevent negative density and negative pressure, two barrier functions, $b_1(\rho) = -\beta_1 \log\rho$ and $b_2(p) = -\beta_2 \log p$, are added to the mass-conservation equation and the total-energy-conservation equation as source terms. The coefficients in the barrier functions are chosen to be $\beta_1 = 10^{-9}$ and $\beta_2 = 10^{-12}$ in this study, and they become zero after the stopping criterion of the Newton iteration is satisfied. Because the coefficients are very small, the barrier functions are negligible in a regular situation. However, if

density or pressure nears zero during the Newton iteration, the corresponding barrier function gives a significantly large function value, resulting in a high slope, and thus the search direction $\Delta \boldsymbol{z}$ goes away from the corresponding boundary, $\rho = 0$ or $p = 0$. The barrier functions with the parabolic step-size algorithm helps the Newton system become stable.

The flow solver that provides us with $\boldsymbol{F}(\boldsymbol{w}; \phi)$ during the Newton iteration is our in-house Reynolds-averaged Navier-Stokes (RANS) solver called "JOE" (Pečnik *et al.* 2012). The JOE solver is a finite-volume collocated compressible-flow solver using the HLLC shock-capturing scheme (Toro *et al.* 1994) and can handle unstructured meshes in three-dimensional space. Its accuracy is second order in space on unstructured meshes if shocks do not occur, but the spatial accuracy reduces to about first order near a shock due to extra dissipation from the HLLC shock-capturing scheme. Turbulent viscosity in the flow is provided by the Wilcox $k - \omega$ RANS model (Wilcox 2006).

The implementation of the Newton iteration shows a reasonable convergence. The iterative process converges in about 10 iterations if the Jacobian matrix $\mathcal{A}_{\boldsymbol{z}}$ is stable, whereas more than 100 iterations are required if the Jacobian matrix is unstable or marginally stable. This is because the condition number of $\mathcal{A}_{\boldsymbol{z}}$ grows as the least-stable eigenvalue of the Jacobian matrix approaches zero. When $\mathcal{A}_{\boldsymbol{z}}$ is only marginally stable, the condition number of $\mathcal{B}_{\boldsymbol{z}}$ also becomes large, deteriorating the convergence of the Newton iteration.

3.2. *Calculation of the Jacobian matrix and evaluation of its eigen-pairs*

The Newton iteration requires the evaluation of the Jacobian matrix $\mathcal{A}_{(\boldsymbol{w};\phi)}$ as well as the evaluation of the vector function $\boldsymbol{F}(\boldsymbol{w}; \phi)$. To compute $\mathcal{A}_{(\boldsymbol{w};\phi)}$, taking into account complex geometry using unstructured meshes as well as shock-capturing via the HLLC scheme, we employ the technique of automatic differentiation (AD) (Griewank 2000). AD is a technique whereby exact derivatives of a function are calculated by computers without truncation errors, and thus it is much more accurate than traditional methods such as finite differences. This technique has already been used in some fluid dynamics applications. For example, Wang *et al.* (2012) applied AD to the JOE flow solver in estimating the probability of unstart of an inviscid scramjet engine. In their study, AD played an important role in producing adjoints that were used to reduce sampling costs.

We rewrote the original code by Wang *et al.* to obtain a better performance since the number of Jacobian evaluations is several orders of magnitude higher than that of Wang *et al.* (2012) due to the Newton iterative procedures. To improve performance, the new implementation takes advantage of modified data structures as well as efficient access to the AD package. As a result, the new code runs over 100 times faster than the original code by Wang *et al.* while giving the same Jacobians.

The eigen-decomposition of the Jacobian matrix $\mathcal{A}_{(\boldsymbol{w};\phi)}$ is obtained by using the Arnoldi iteration developed in the SLEPc parallel linear-algebra package (Hernandez *et al.* 2005), because $\mathcal{A}_{(\boldsymbol{w};\phi)}$ is sparse and unsymmetric. However, the convergence of the nominal Arnoldi method is undesirable when the eigenvalues of $\mathcal{A}_{(\boldsymbol{w};\phi)}$ are distributed in an ill-favored way or the size of the Jacobian matrix is not small (in this study, the size is about 1.5×10^6 by 1.5×10^6). Therefore, the shift-and-invert spectral-transformation algorithm(Jia & Zhang 2002) is adopted for improved convergence. In this algorithm, the original eigen problem of $\mathcal{A}\boldsymbol{y} = \lambda \boldsymbol{y}$ is modified to

$$(\mathcal{A} - \sigma I)^{-1} \boldsymbol{y} = (\lambda - \sigma)^{-1} \boldsymbol{y}. \tag{3.1}$$

The global-mode $\boldsymbol{y}$ in this modified problem is the same as the global mode of the original

problem, and a proper choice of the shift σ accelerates the convergence of the iterative process for eigenvalues near σ. Hence, in this study, the least-stable eigenvalue λ_1 is first found using the nominal Arnoldi iteration, and other eigenvalues are found by the shift-and-invert spectral-transformation algorithm with $\sigma = 1/2\lambda_1$. The matrix inverse of $(\mathcal{A} - \sigma I)$ is found by the LU decomposition that is provided by the parallel direct sparse solver, MUMPS (Amestoy *et al.* 2000).

3.3. *Scramjet configuration*

The scramjet model in the study is adopted from the model scramjet in the series of the HyShot II experiments. The successful flight test was performed at the University of Queensland (Smart *et al.* 2006) followed by ground experiments both at the University of Queensland (Frost *et al.* 2009) and in the High Enthalpy shock tunnel Göttingen (HEG) facility of the German Aerospace Center (DLR) (Gardner *et al.* 2004; Hannemann *et al.* 2010; Laurence *et al.* 2013, 2015). In the HyShot II flight experiment, the free-stream properties are $M = 7.8$, $T = 242$ K, and $p = 1711$ Pa when HyShot II was in an altitude of 27 km, and the angle of attack of the vehicle at this location was 3.6°. These free-stream conditions were also investigated in Gardner *et al.* (2004), and the later experimental studies at DLR aimed at an altitude of 28 km, using similar free-stream conditions. This series of experimental studies revealed data sets in unstart physics, but the detailed analysis of the scramjet model still relied on one-dimensional analysis or simulation data of the same geometry because access to the comprehensive flow field was limited in the experiments.

The scramjet model in the experiments includes an 18° intake ramp, a 0.3 m-long constant-area combustor, and an expansion nozzle. However, because the supersonic flow on the intake ramp is not affected by the downstream changes in the combustor-nozzle system during the unstrart process, the intake ramp is not included in this study. Figure 1 gives the comparison between the full geometry and the reduced geometry. The contour levels in the figure represent velocity divergence, showing compression regions as black and expansion regions as white. Therefore, shock waves are shown as black lines, whereas white regions show expansion waves. Figure 1(a) shows the two-dimensional flow field of the full geometry with $\phi = 0$, and the computational mesh is taken from the computational study by Pečnik *et al.* (2012) that considered the entire intake-combustor-nozzle system. In this full-geometry calculation, the properties of the free stream at the domain inlet are matched with the corresponding values in the ground experiment by Gardner *et al.* (2004), and the walls are isothermal at 300 K. The intake ramp starts at $x = 0$ m, where x is the horizontal coordinate, and the leading edge of the lower wall of the combustor is located at $x_{\text{inlet}} = 0.35$ m. Because the combustor is 0.3 m long, the following expansion nozzle starts at $x_{\text{throat}} = 0.65$ m. On the other hand, the inlet of this reduced domain is located at about 4.3 mm upstream of x_{inlet}, as shown in Figure 1(b). On the combustor walls, the grid size in the wall-normal direction is fine enough to capture the growth of boundary layers on these walls. The number of grid points in this reduced domain is 0.21×10^6.

The flow profiles at the domain inlet in Figure 2(b) are taken from the same grid locations in the full domain simulation in Figure 2(a), and the flow profiles are applied to the reduced domain as the Dirichlet boundary condition. Figure 2 highlights the two computational domains near x_{inlet}. The Mach number at the reduced-domain inlet is approximately $M = 2.62$, and the flow direction becomes parallel to the upper wall and lower wall of the combustor before entering into the combustor. At the inlet of the combustor ($x_{\text{inlet}} = 0.35$ m), two oblique shocks are formed due to the round shape of the

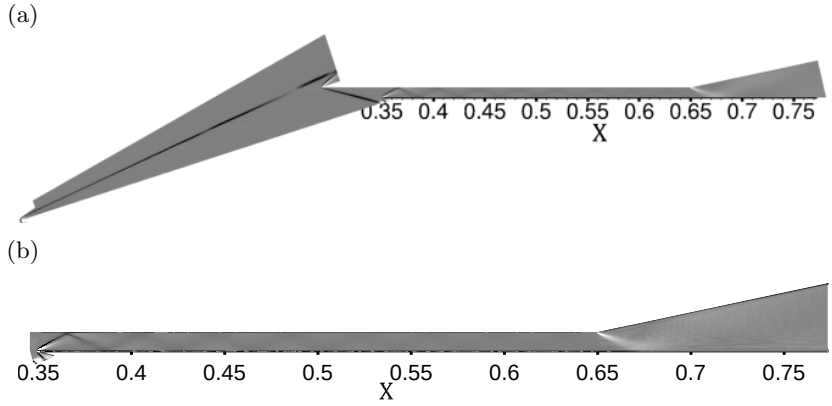

FIGURE 1. Divergence contours at $\phi = 0$: (a) full computational domain; (b) reduced domain. Black regions indicate negative divergence (compression); white regions indicate positive divergence (expansion). The scales in (a) and (b) are not the same.

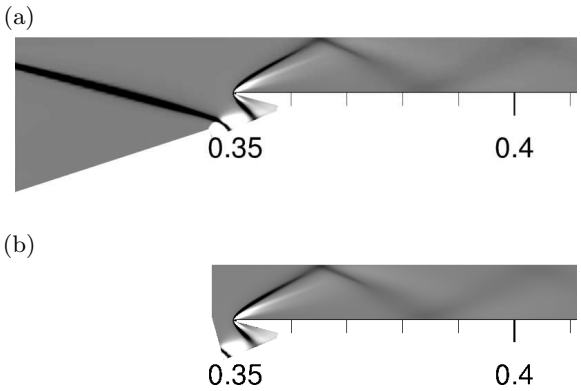

FIGURE 2. Divergence contours near the combustor inlet at $\phi = 0$: (a) full computational domain, (b) reduced domain. Black regions indicate negative divergence (compression); white regions indicate positive divergence (expansion).

lower-wall leading edge. The upper oblique shock that comes into the combustor reflects from the combustor walls, generating an oblique-shock train.

In this study, the heat from combustion is released to the scramjet system by a surrogate model. In the HyShot II experiments, hydrogen fuel was injected in the wall-normal direction at 58 mm downstream of the leading edge of the combustor, and the fuel was mixed with the incoming air and combusted afterward. The heat release from combustion is followed by a pressure rise along the stream-wise direction, and excessive heat release results in unstart. However, capturing detailed combustion chemistry requires excessive computational costs, and thus a low-order model is required when a large number of computations is needed to obtain the solution curve. Low-order models have been proposed in scramjet studies, and many of them are one-dimensional models. For example, Mitani *et al.* (2003) used one-dimensional simulations to predict thrust of two different scramjets, and the thrust prediction by the simple simulations agreed reasonably well with the experimental measurements until the fuel equivalence ratio exceeded the unstart limit.

Symbol	Definition	Baseline value
f_{st}	Stoichiometric fuel/air ratio	0.028
H_f	Fuel heating value of hydrogen fuel	120 MJ/kg
L_c	Combustor length	0.368 m
K_c	Fraction of completed combustion	0.95
D_c	Shape parameter	0.75
C_c	Shape parameter	$-log(1-K_c)^{1/D_c}$
X_c	Combustion ignition position	0.418 m

TABLE 1. Parameters used in the heat-release model

In the study of HyShot II by Laurence *et al.* (2013), the unstart limit in the equivalence ratio was successfully predicted by a one-dimensional model based on Rayleigh's flow assumptions, and the authors reported that the onset of unstart is sensitive to the total heat release from the combustion. Doolan & Boyce (2008) used a quasi one-dimensional mixing-and-combustion model to estimate the performance of the ground experiment by Boyce *et al.* (2000), and the model output agreed well with the experimental data. Similarly, Tourani (2011) showed that one-dimensional simulations can closely predict the overall evolution of the flow in the scramjet combustor as shown in the study of Oevermann (2000).

The heat-release model in this study is the model proposed by Wang *et al.* (2012). In this model, heat is added to the system through a volumetric term given in the following formula:

$$Q = \phi f_{st} H_f m_{air} \eta(x/L_c), \tag{3.2}$$

where ϕ is the heat-release rate, and $\eta(x/L_c) = 1 - e^{-(C_c x/L_c)^{D_c}}$ is the heat distribution function along the stream-wise direction. The parameters in the above equation are given in Table 1. Using this model, the heat release from the combustion in the HyShot II experiment is modeled, whereas the boundary layer and the oblique shock train in the combustor are captured in detail in the two-dimensional flow simulations.

4. Results

4.1. *Solution curve*

The solution curve of the two-dimensional HyShot II is calculated using the pseudo-arclength continuation technique, and a part of the curve is given in Figure 3. The horizontal axis of the plot is the heat-release rate ϕ given in Eq. (3.2), and the vertical axis is the average density in the combustor-nozzle system that was an effective metric to represent the unstart in a simple converging-diverging nozzle in Jang *et al.* (2012). The numerical continuation starts from a converged steady-state RANS solution at $\phi = 0.3970$ using the nominal JOE solver, and the solution curve proceeds with the aid of the numerical continuation method. The initial step size in ϕ is $\Delta\phi = 2.382 \times 10^{-3}$, and $\Delta\phi$ changes adaptively at each point on the solution curve to get the minimum number of iterations in the Newton method. Near P2 in Figure 3, for example, $\Delta\phi$ is reduced to 8.922×10^{-5} because the Newton method requires an excessive number of iterations if $\Delta\phi$ is not reduced near this solution point. When ϕ is low, the solution curve in Figure 3 is almost a linear function of ϕ. However, as the solution proceeds on the solution curve

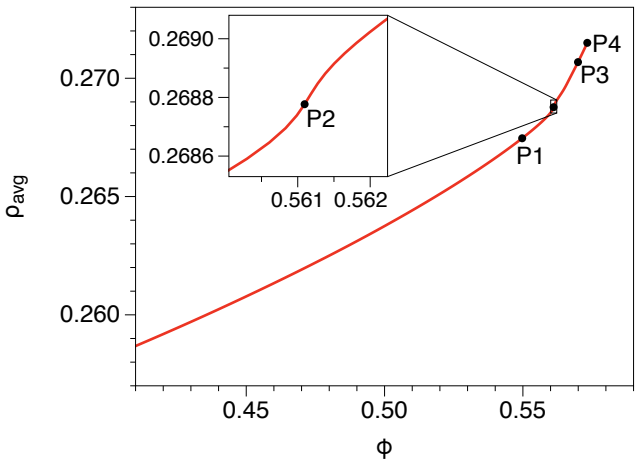

FIGURE 3. Solution curve of the 300 mm case.

from P1 to P2 in Figure 3, the slope of the curve becomes steeper, forming an inflection point at P2.

At the infection point P2, a weak shock structure is first formed near the throat, and as ϕ increases from P2, the shock structure moves upstream and becomes stronger. The divergence contours near the throat (x_{th}) at the four solution points shown in Figure 4 show the evolution of the shock structure. The enlarged images in Figure 4 clearly show the evolution of the normal shock near the throat. In the divergence contours at P2 given in Figure 4(b), a weak shock structure is formed near $x = 0.643$ m, that is not shown at a lower ϕ (e.g., the divergence contours at P1 given in Figure 4(a)). If a higher value of ϕ is applied, the normal shock becomes stronger, and its position moves upstream, as shown in Figure 4(c) and (d).

This result is similar to the observations in the ground experiments by Laurence *et al.* (2013). In their experiment, pressure was measured by pressure tabs on both the injector-side wall and the cowl-side wall, and the location of a sudden rise in the wall-pressure distribution was also stationary in time. The sudden rise in wall-pressure is believed to be related to the leading shock in the unstart structure, and the location of the sudden rise was a function of the fuel equivalence ratio in the experiment (ϕ_{exp}). When $\phi_{exp} \simeq 0.66$, for example, the location of the leading shock moved to just downstream of the injector, and there was a noticeable uncertainty of the leading-shock location at a high value of ϕ_{exp} in their experiments. If ϕ_{exp} increases to about 1.1, the location of the pressure jump passes the injector, but the exact position was not reported because pressure in the upstream from the injector was not measured.

Figure 5 shows the Mach number contours at the four different points on the solution curve. In the Mach number contours at P1, the flow is supersonic in most of the region between the walls, and the subsonic zones are confined in the boundary layer on the walls. When ϕ is increased to 0.5611 (P2), the subsonic zone becomes thicker, especially downstream of the normal shock. If more heat is added to the system, the subsonic zones grow to the centerline of the combustor, and they finally form a full subsonic band that spans the total height of the duct. The first formation of the full subsonic band is found at P3, and a wider band is observed at a more upstream location as ϕ increases.

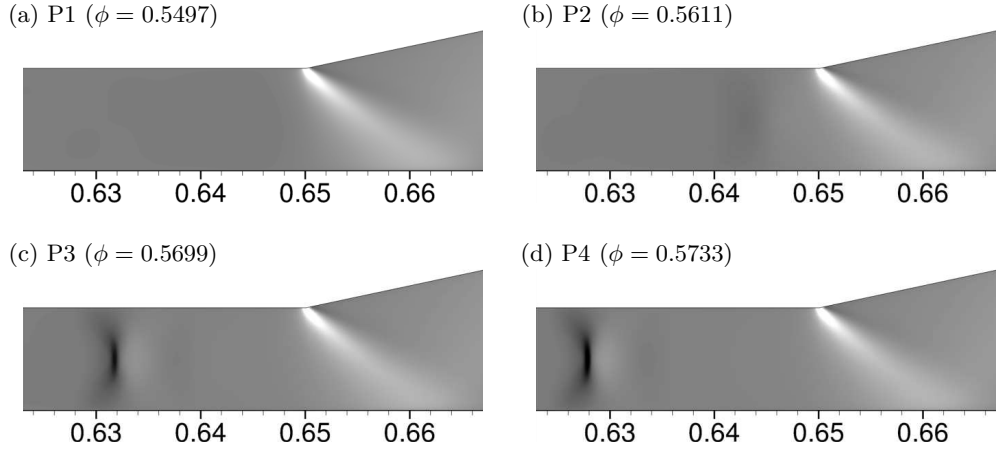

FIGURE 4. Velocity divergence contours near $x_{\text{th}} = 0.65$: (a) P1 in Figure 3 ($\phi = 0.5497$), (b) P2 ($\phi = 0.5611$), (c) P3 ($\phi = 0.5699$), (d) P4 ($\phi = 0.5733$). Black regions indicate negative divergence (compression); white regions indicate positive divergence (expansion).

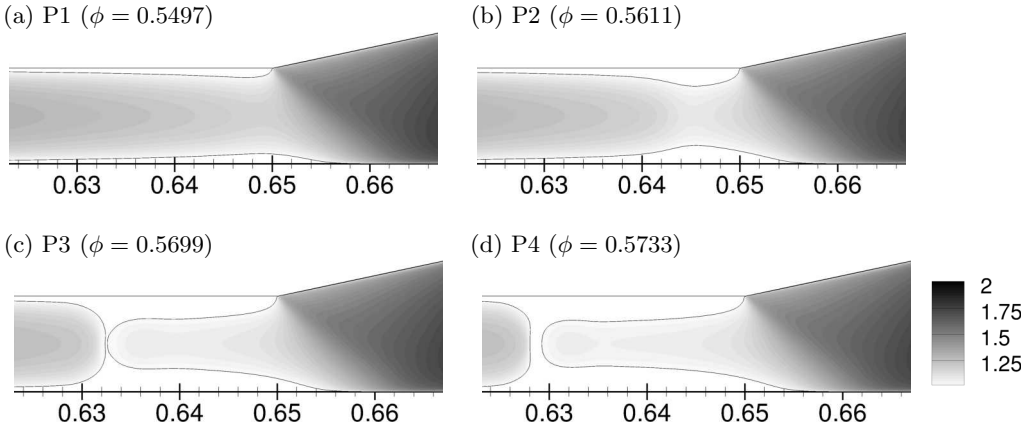

FIGURE 5. Mach number contours near $x_{\text{th}} = 0.65$ at four different points on the solution curve given in Fig 3: (a) P1 in Figure 3 ($\phi = 0.5497$), (b) P2 ($\phi = 0.5611$), (c) P3 ($\phi = 0.5699$), (d) P4 ($\phi = 0.5733$). White regions are subsonic ($M < 1$).

4.2. *Linear dynamics*

The eigenvalues of the Jacobian matrix $\mathcal{A}_{(\boldsymbol{u},\phi)}$ at four points (P1, P2, P3, and P4) on the solution curve are given in Figure 6. Because eigen-decomposition requires significant computing resources, only 13 eigenvalues with the largest real part $(\lambda_1, \cdots, \lambda_{13})$ are calculated. Of the 13 eigenvalues, 5 eigenvalues are purely real, whereas the other 8 eigenvalues form four complex-conjugate pairs. At P1, the real part of the least-stable eigenvalue λ_1 is about -1.0×10^{-6}, whose absolute value is an order of magnitude higher than the λ_1's at the other three solution points. In addition, λ_1 at P1 is close to the other eigenvalues $(\lambda_2, \cdots, \lambda_{13})$, but when ϕ increases to the value at P2, λ_1 is separated from the other eigenvalues, approaching zero. At P3 and P4, the distance between λ_1 and λ_2 is still considerably larger than that at P1. Therefore, as ϕ increases, the mode associated with λ_1 can survive longer, while the other modes decay quickly. This means that this slow dynamics of λ_1 is associated with the evolution of the moving-shock structure.

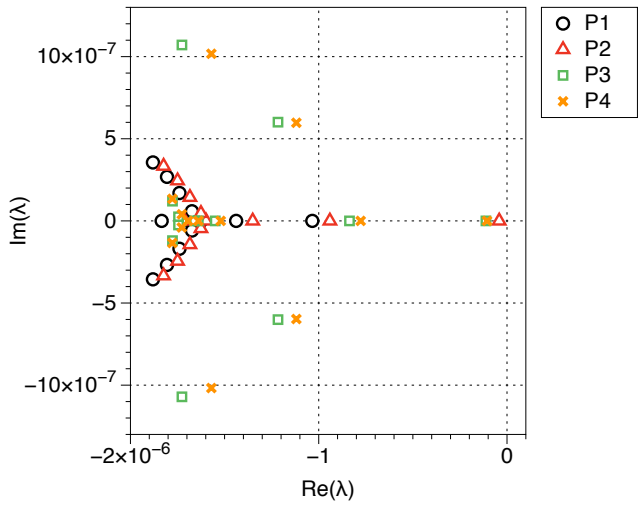

FIGURE 6. 13 eigenvalues with the largest real parts, taken at four different points on the solution curve given in Fig 3. Black circles = P1; red triangles = P2; green squares = P3; orange crosses = P4.

Furthermore, λ_1 at P2 comes close to zero, and thus the system is marginally stable when the shock structure is first formed.

The least-stable direct global mode at the inflection point (P2) is shown in Figure 7 along with the divergence contours in Figure 7(a) that indicate the location of the normal shock at $x \simeq 0.642$. In the contour plots in the Figure 7(b), (c), and (d), the amplitude and the sign are arbitrary because of normalization. Figure 7 (b) exhibits the vector field of $(\boldsymbol{y}_{1,u_1}, \boldsymbol{y}_{1,u_2}) = (\boldsymbol{y}_{1,\rho u_1}/\rho, \boldsymbol{y}_{1,\rho u_2}/\rho)$. The vector field shows two big circular motions behind the shock, and they are symmetric with respect to the centerline between the upper and lower walls. The circular motions near the walls are directed to downstream, and they merge into one upstream motion on the centerline. Figure 7 (c) and (d) show the contour plots of $\boldsymbol{y}_{1,\rho}$ and $\boldsymbol{y}_{1,\rho E}$, respectively. In both plots, a noticeable peak is found on the centerline downstream of the normal shock, and the shape of the peak is an oval whose long axis is oriented along the wall-normal direction.

5. Conclusions

The equilibrium solution curve of the two-dimensional HyShot II is found as a function of the heat-release rate ϕ by the pseudo-arclength technique with Newton iteration. At the inflection point on the solution curve, a shock structure is first found, and the shock structure moves upstream with increasing ϕ, as previously observed in a ground experiment of HyShot II. The linear-system analysis reveals the separation of slow and fast dynamics, and visualization of the least-stable global mode at the inflection point depicts the strengthening or weakening mechanisms of the shock structure.

Based on the onset dynamics of the shock structure found in this study, unstart-mitigation mechanisms can be suggested in connection with the linearized dynamics. In particular, the adjoint global modes of the linearized system are related to the receptivity of the system to perturbations. Therefore, the optimal control mechanisms can be found by considering both the direct global modes and the adjoint global modes. Calculating

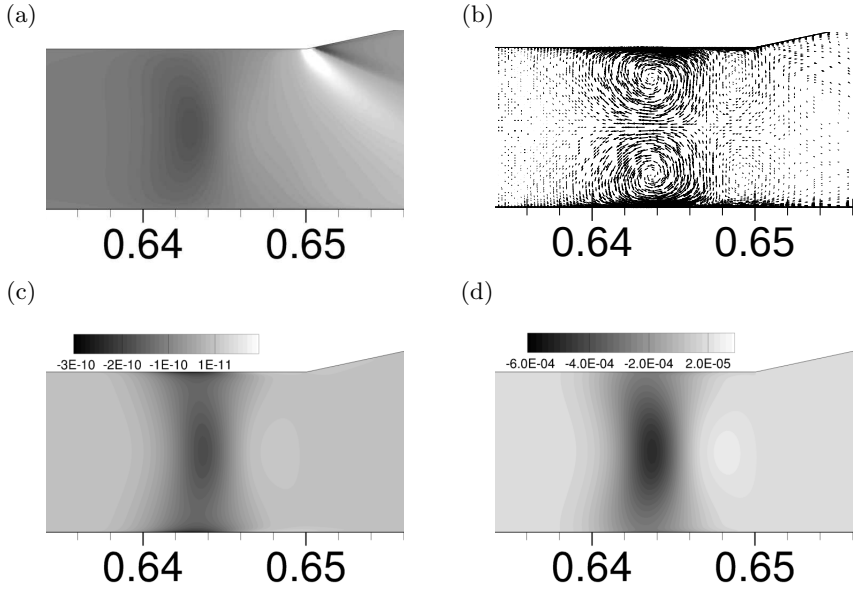

FIGURE 7. The least-stable global mode at the inflection point P2 (enlarged near the throat): (a) divergence of velocity field in the base flow field (black=compression, white=expansion), (b) vector field of $(\boldsymbol{y}_{1,u_1}, \boldsymbol{y}_{1,u_2})$, (c) density $\boldsymbol{y}_{1,\rho}$, (d) total energy $\boldsymbol{y}_{1,\rho E}$.

the adjoint global modes and finding the unstart-mitigation mechanisms are the subjects of the ongoing study.

Acknowledgments

This investigation was funded by DOE/NNSA and AFOSR.

REFERENCES

ALLGOWER, E. L. & GEORG, K. 1997 *Numerical Path Following*, *In Handbook of Numerical Analysis*, vol. 5. North-Holland.

AMESTOY, P. R., DUFF, I. S. & L'EXCELLENT, J. Y. 2000 Multifrontal parallel distributed symmetric and unsymmetric solvers. *Comput. Methods in Appl. Mech. Eng.* **184**, 501–520.

BOYCE, R. R., PAULL, A., STALKER, R. J., WENDT, M., CHINZEI, N. & MIYAJIMA, H. 2000 Comparison of supersonic combustion between impulse and vitiation-heated facilities. *J. Propul. Power* **16** (4), 710–717.

CHAN, T. & KELLER, H. 1982 Arc-length continuation and multigrid techniques for nonlinear elliptic eigenvalue problems. *SIAM J. Sci. Stat. Comp.* **3** (2), 173–194.

DOOLAN, C. J. & BOYCE, R. 2008 A quasi-one-dimensional mixing and combustion code for trajectory optimization and design studies. *AIAA Paper* 2008-2603.

FROST, M. A., GANGURDE, D. Y., PAULL, A. & MEE, D. J. 2009 Boundary-layer separation due to combustion-induced pressure rise in a supersonic flow. *AIAA J.* **47** (4), 1050–1053.

GARDNER, A., STEELANT, J., PAULL, A. & HANNEMANN, K. 2004 Ground testing of

the Hyshot supersonic combustion flight experiment in HEG and comparison with flight data. *AIAA Paper* 2004-3345.

Griewank, A. 2000 *Evaluating Derivatives, Principles and Techniques of Algorithmic Differentiation*. SIAM.

Hannemann, K., Karl, S., Schramm, J. M. & Steelant, J. 2010 Methodology of a combined ground based testing and numerical modelling analysis of supersonic combustion flow paths. *Shock Waves* **20**, 353–366.

Hernandez, V., Roman, J. E. & Vidal, V. 2005 SLEPc: A scalable and flexible toolkit for the solution of eigenvalue problems. *ACM Trans. Math. Software* **31** (3), 351–362.

Jang, I., Nichols, J. W. & Moin, P. 2012 Bifurcation analysis of scramjet unstart. *Annual Research Briefs*, Center for Turbulence Research, Stanford University, pp. 153–160.

Jia, Z. & Zhang, Y. 2002 A refined shift-and-invert Arnoldi algorithm for large unsymmetric generalized eigen problems. *Comput. Math. Applic.* **44**, 1117–1127.

Keller, H. B. 1977 *Numerical Solution of Bifurcation and Nonlinear Eigenvalue Problems*. Academic Press.

Kelley, C. T. 1995 *Iterative Methods for Linear and Nonlinear Equations*. SIAM.

Korkegi, R. H. 1975 Comparison of shock induced two- and three-dimensional incipient turbulent separation. *AIAA J.* **13** (4), 534–535.

Laurence, S. J., Karl, S., Schramm, J. M. & Hannemann, K. 2013 Transient fluid-combustion phenomena in a model scramjet. *J. Fluid Mech.* **722**, 85–120.

Laurence, S. J., Lieber, D., Schramm, J. M., Hannemann, K. & Larsson, J. 2015 Incipient thermal choking and stable shock-train formation in the heat-release region of a scramjet combustor. Part I: Shock-tunnel experiments. *Combust. Flame* **162**, 921–931.

Mitani, T., Tomioka, S., Kanda, T., Chinzei, N. & Kouchi, T. 2003 Scramjet performance achieved in engine tests from M4 to M8 flight conditions. *AIAA Paper* 2003-7009.

Oevermann, M. 2000 Numerical investigation of turbulent hydrogen combustion in a scramjet using flamelet modeling. *Aerosp. Sci. Technol.* **4** (7), 463–480.

Pečnik, R., Terrapon, V. E., Ham, F., Iaccarino, G. & Pitsch, H. 2012 Reynolds-Averaged Navier-Stokes simulations of the Hyshot II scramjet. *AIAA J.* **50** (8), 1717–1732.

Smart, M. K., Hass, N. E. & Paull, A. 2006 Flight data analysis of the hyshot 2 scramjet flight experiment. *AIAA J.* **44** (10), 2366–2375.

Toro, E., Spruce, M. & Speares, W. 1994 Restoration of the contact surface in the HLL-Riemann solver. *Shock Waves* **4** (1), 25–34.

Tourani, C. 2011 Computational simulation of scramjet combustors a comparison between quasi-one dimensional and 2-D numerical simulations. *AIAA Paper* 2011-2285.

Wang, Q., Duraisamy, K., Alonso, J. & Iaccarino, G. 2012 Risk assessment of scramjet unstart using adjoint-based sampling methods. *AIAA J.* **50** (3), 581–592.

Wilcox, D. C. 2006 *Turbulence Modeling for CFD*. DCW Industries.